


ARTICLE OPEN

Confinement of magnetism in atomically thin $\text{La}_{0.7}\text{Sr}_{0.3}\text{CrO}_3/\text{La}_{0.7}\text{Sr}_{0.3}\text{MnO}_3$ heterostructuresSanaz Koohfar¹, Alexandru B. Georgescu², Aubrey N. Penn³, James M. LeBeau³, Elke Arenholz⁴ and Divine P. Kumah¹ 

At crystalline interfaces where a valence-mismatch exists, electronic, and structural interactions may occur to relieve the polar mismatch, leading to the stabilization of non-bulk-like phases. We show that spontaneous reconstructions at polar $\text{La}_{0.7}\text{Sr}_{0.3}\text{MnO}_3$ interfaces are correlated with suppressed ferromagnetism for film thicknesses on the order of a unit cell. We investigate the structural and magnetic properties of valence-matched $\text{La}_{0.7}\text{Sr}_{0.3}\text{CrO}_3/\text{La}_{0.7}\text{Sr}_{0.3}\text{MnO}_3$ interfaces using a combination of high-resolution electron microscopy, first principles theory, synchrotron X-ray scattering and magnetic spectroscopy and temperature-dependent magnetometry. A combination of an antiferromagnetic coupling between the $\text{La}_{0.7}\text{Sr}_{0.3}\text{CrO}_3$ and $\text{La}_{0.7}\text{Sr}_{0.3}\text{MnO}_3$ layers and a suppression of interfacial polar distortions are found to result in robust long-range ferromagnetic ordering for ultrathin $\text{La}_{0.7}\text{Sr}_{0.3}\text{MnO}_3$. These results underscore the critical importance of interfacial structural and magnetic interactions in the design of devices based on two-dimensional oxide magnetic systems.

npj Quantum Materials (2019)4:25; <https://doi.org/10.1038/s41535-019-0164-1>

INTRODUCTION

Structural, electronic, and magnetic interactions at the interfaces between thin films of crystalline polar transition metal perovskites have led to the realization of a wide range of physical phenomena not found in the bulk constituent materials. These exotic phenomena, which include, two-dimensional electronic gases, interfacial magnetism and superconductivity and orbital ordering are driven by interfacial chemical, structural, electronic, and orbital reconstructions, which serve to alleviate the polar mismatch at these interfaces.^{1,2} A consequence of these reconstructions is that significant deviations in the atomic-scale structural and electronic properties of atomic layers adjacent to the polar interfaces arise. Owing to the strong coupling of the structural, electronic, and magnetic properties in these materials, detrimental effects may be induced in layers close the interface leading to strong thickness-dependent physical properties.^{3–5} To confine the functional properties of transition metal perovskites to two-dimensions in order to realize exciting phenomena associated with quantum confinement and engineer device architectures including spin-tunnel junctions, understanding and controlling these interfacial interactions is crucial. In addition, in multiferroic heterostructures where the magnetoelectric coupling effect is confined to interfacial layers,⁶ reducing the thicknesses of the component layers to the order of a unit cell will lead to an enhanced coupling of ferroic order parameters.

An important system that displays thickness-dependent transitions related to interfacial interactions is the LaSrMnO_3 (LSMO)/ SrTiO_3 (STO) interface. LSMO films have been explored for their half-metallic properties and colossal magnetoresistance effects with applications in spintronic devices.⁶ The magnetic and electronic properties are related to the Mn–O bond properties in neighboring unit cells through double exchange interactions and Jahn–Teller effects.⁷ Distortions to the Mn–O bond angle achieved

by chemical substitution and strain results in a modulation of the magnetic and electronic phases.⁸ When grown as epitaxial thin films, properties of LSMO can be coupled to other functional oxides including ferroelectric and superconducting perovskite transition metal oxides.^{6,9,10}

LSMO films have been reported to undergo a ferromagnetic to paramagnetic transition for film thicknesses below 4–10 unit cells (uc) when grown on lattice-matched STO substrates.^{3,11} The thickness-dependent phase transition has been attributed to interfacial interactions driven by the polar mismatch between the two materials. These interactions include interfacial ionic intermixing, which leads to deviations in the composition of interfacial LSMO layers,^{12,13} interfacial charge transfer evidenced by X-ray absorption spectroscopy and electron microscopy measurements, and ferro-distortive ionic displacements.^{14–16}

To eliminate the interfacial interactions that lead to suppressed magnetism, we show that the insertion of $\text{La}_{1-x}\text{Sr}_x\text{CrO}_3$ (LSCO) spacer layers at LSMO interfaces removes polar structural distortions observed at LSMO interfaces¹⁴ and couples to the lattice symmetry of LSMO, leading to robust ferromagnetism down to 2 uc in LSCO (M uc)/LSMO (N uc)/LSCO (M uc) (M/N/M) heterostructures grown on (001)-oriented STO substrates by molecular beam epitaxy. The role of the LSCO spacer is twofold: (1) By matching the La/Sr ratio of the LSCO to the LSMO film, the polar mismatch at the LSMO interface is effectively removed and (2) LSCO that has a $R\bar{3}c$ symmetry with $a'a'a'$ rotations (160° Cr–O–Cr bond angle, 3.88 Å pseudocubic lattice constant)¹⁷ couples to the oxygen octahedral rotations in LSMO alleviating the oxygen octahedral mismatch.^{18,19} In addition, we observe an antiferromagnetic (AF) exchange interaction between the Cr and Mn ions at the LSMO/LSCO interface. Using a combination of temperature-dependent magnetometry, picometer-scale synchrotron X-ray based /structural characterization and element-specific magnetic

¹Department of Physics, North Carolina State University, Raleigh, NC 27695, USA; ²Center for Computational Quantum Physics, Flatiron Institute, 162 5th Avenue, New York, NY 10010, USA; ³Department of Materials Science and Engineering, North Carolina State University, Raleigh, NC 27695, USA and ⁴Advanced Light Source, Berkeley, CA 94720, USA
Correspondence: Divine P. Kumah (dpkumah@ncsu.edu)

Received: 11 January 2019 Accepted: 5 May 2019

Published online: 29 May 2019

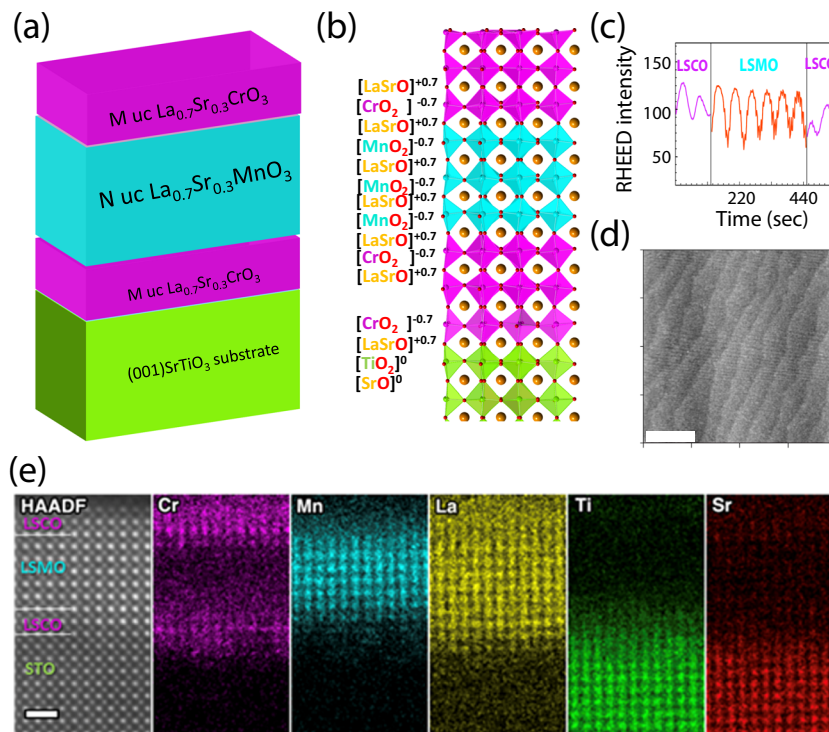


Fig. 1 Tuning the valence-mismatch at manganite interfaces. **a** Schematic of $\text{La}_{0.7}\text{Sr}_{0.3}\text{CrO}_3$ (M)/ $\text{La}_{0.7}\text{Sr}_{0.3}\text{MnO}_3$ (N)/ $\text{La}_{0.7}\text{Sr}_{0.3}\text{CrO}_3$ (M) (M/N/M) heterostructures grown by molecular beam epitaxy on (001)-oriented SrTiO_3 substrates. **b** Schematic of a 3/3/3 structure showing the net charges in the AO (A = La,Sr) and BO_2 (B = Ti,Mn,Cr) layers. **c** RHEED oscillations recorded in-situ during the growth of a 2/6/2 heterostructure. **d** The corresponding atomic force microscope image of the surface topography of the 3/3/3 heterostructure exhibiting unit cell high terrace steps. The scale bar represents 500 nm. **e** Representative HAADF-STEM image and EDS map of nominally 2/6/2 LSCO/LSMO. The scale bar represents 1 nm

spectroscopy, we demonstrate the enhancement of ferromagnetic ordering in ultrathin LSMO films, and the stabilization of bulk-like ferromagnetism in LSMO layers as thin as 2 uc (0.8 nm). The results are confirmed by first principles theory.

RESULTS

Atomic-layer synthesis

LSMO films and LSCO (M)/LSMO (N)/LSCO (M) (M/N/M) heterostructures and [LSCO (M)/LSMO (N)] superlattices were synthesized by plasma-assisted oxide molecular beam epitaxy at a growth temperature of 800°C. The LSMO thickness, N, was varied from 2 to 10 uc, whereas the LSCO thickness, M, was fixed at either 2 or 3 uc to be above the decay length for surface polar distortions observed for LSMO¹⁴ and LaNiO_3 ²⁰ films. A schematic of the heterostructures is shown in Fig. 1a. As shown in Fig. 1b, the LSCO layers possess the same ± 0.7 net charge stacking along the growth direction. Hence, no polar discontinuity exists at the LSMO top and bottom interfaces. RHEED oscillations are observed for all the layers indicative of layer-by-layer growth as shown in Fig. 1c. The surface morphology of the films were characterized by atomic force microscopy. A representative atomic force microscope image is shown in Fig. 1d for the 3/3/3 sample with a surface roughness of <1 unit cell.

High-resolution electron microscopy measurements

The aberration-corrected high-angle annular dark field-scanning transmission electron microscopy (HAADF-STEM) (Z-contrast) image in Fig. 1e shows the 2/6/2 heterostructure. Energy-dispersive x-ray spectroscopy (EDS) chemical maps reveal some chemical intermixing within a unit cell between Mn and Cr layers and Ti migration across the LSCO/STO interface.²¹ In contrast, the

La signal drops abruptly at the interface. Electron energy loss spectroscopy (EELS) was also performed in the STEM to track relative variations in Mn and Cr oxidation state across the film with the $L_{3/2}$ white line ratio according to the method described by Tan et al.²²

Magnetization measurements

The magnetic properties of the LSMO thin films and M/N/M heterostructures and [M/N] superlattices were characterized using a Quantum Design SQUID system. The magnetization curves normalized to the Mn are shown as a function of field and temperature at 10 K for $M = 3$ and $N = 2, 3, 4, 6$, and 10 in Fig. 2a, b, respectively. Temperature-dependent curves were recorded after field cooling the samples in a 1 Tesla field applied in-plane. As will be discussed later, the magnetization in the LSMO sublattice is determined to be closed to bulk, and the reduced net SQUID magnetization as the LSMO thickness decreases is related to the contribution of anti-parallel spins in the LSCO layers resulting from AF interactions between the LSMO and LSCO layers.

In contrast to the single layer LSMO films, the 3/N/3 heterostructures remain ferromagnetic down to $N = 2$. Inserting 3 uc LSCO at the LSMO top and bottom interfaces results in ferromagnetic ordering below ~150 K compared with the 2 uc LSMO films grown directly on STO, which remains paramagnetic down to 2 K. To verify that the magnetism in the heterostructures is not within the LSCO layers alone, the magnetization for a 6 uc LSCO layer was measured and found to be similar to the STO substrate down to 2 K as shown in Figure S1 of the supplementary materials. The results for the LSCO film are consistent with bulk LSCO which is a G-type antiferromagnet.¹⁷

We further elucidate the magnetic coupling at LSCO/LSMO interface by measuring the magnetization hysteresis loops after

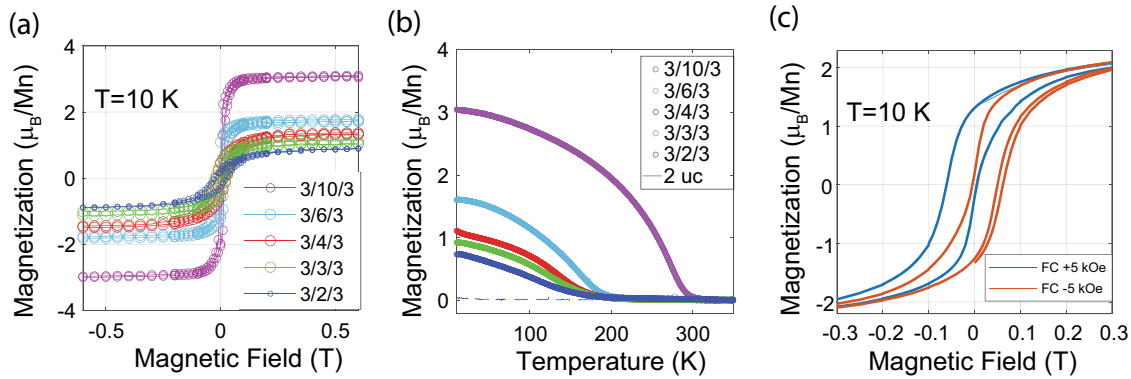


Fig. 2 Effect of interface engineering on ferromagnetic ordering in LSCO (3)/LSMO (N)/LSCO (3) heterostructures. **a** Total magnetic moment per Mn as a function of applied magnetic field for 3/N/3 LSCO structures measured at 10 K. The diamagnetic contribution of the SrTiO₃ substrate has been subtracted. **b** Comparison of temperature-dependent magnetization for a 2 uc LSMO film and 3/N/3 heterostructures grown on (001) oriented SrTiO₃ where $N = 2, 3, 4, 6, 10$ unit cells. The curves are measured on warming in an applied in-plane field of 1 kOe. **c** Magnetic hysteresis loops of a [LSCO (2)/LSMO (4)] \times 6 superlattice measured at 10 K by SQUID. The sample was cooled down from the room temperature in the presence of ± 0.5 T magnetic field

cooling down the sample in ± 0.5 T applied in-plane field. Figure 2c demonstrates the presence of an exchange bias for a [LSCO (2)/LSMO (4)] \times 6 superlattice. There is a negative (positive) shift in the hysteresis loop when a positive (negative) field has been applied, indicating reversible switching of exchange bias. The exchange bias field is 332 Oe for both positive and negative field-cooled hysteresis loops.^{23,24}

X-ray circular dichroism measurements

To further confirm that the observed ferromagnetism in the 3/N/3 heterostructures occurs in the LSMO layers, we performed element-specific X-ray magnetic circular dichroism (XMCD) measurements at the Mn and Cr L_{2,3} absorption edges at 4.0.2 beamline at the Advanced Light Source using total electron yield. The absorption spectra at the Cr and Mn edges are consistent with previous measurements for La_{1-x}Sr_xCrO₃²¹ and La_{1-x}Sr_xMnO₃ for $x = 0.3$. The difference between the X-ray absorption spectra measured with right (ρ^+) and left (ρ^-) circular-polarized light yields element-specific magnetic information for the Mn and Cr ions. The XMCD measurements were confirmed by switching the magnetic field direction. XMCD with a 0.5 Tesla in-plane field at 15 K are shown in Fig. 3a, b at the Mn and Cr L-edges, respectively, for a 3/3/3 sample. Dichroic signals were observed at the Mn and Cr edges, indicating magnetic ordering on both the Mn and Cr sublattices. The XMCD hysteresis loop measured at the Mn L-edge in Fig. 3c confirms that the LSMO layer is ferromagnetic. The dichroic signal at the Cr L-edge, whereas weak, exhibits an identical field dependence to the results at the Mn edge but in the opposite direction as shown in Fig. 3d. We conclude from the similarity of the hysteresis loops at the Cr and the Mn L-edges (Figure S2a in Supplementary Materials) that the magnetism in the LSCO is an interfacial effect, i.e., the magnetism in the LSCO layer is induced by the proximity to the ferromagnetic LSMO layer. The induced spin alignment anti-parallel to the applied magnetic field in the LSCO layers is confined to the LSMO/LSCO interface. The measured XMCD signal for Cr is five times smaller than Mn, suggesting that the additional LSCO layers (away from the interface) in the 3/N/3 heterostructures are AF as expected for bulk LSCO.

The temperature dependence of the XMCD signal for a 3/6/3 heterostructure is shown in Fig. 3e at the Mn L-edge. A reduction in the XMCD signal is observed as the temperature is increased from 80 K to 300 K. The magnitude of the XMCD intensities at the Cr and Mn L-edges are compared as a function of temperature in Fig. 3f for the 3/6/3 sample. At both edges, a transition to a paramagnetic state is observed at ~ 200 K in agreement with the

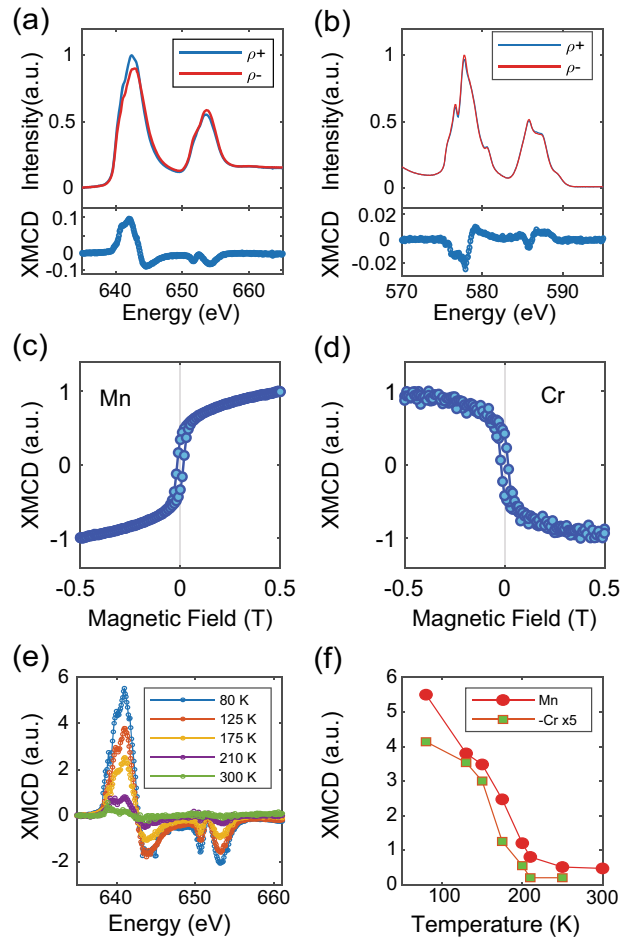


Fig. 3 Magnetic properties of LSCO (M)/LSMO (N)/LSCO (M) (M/N/M) heterostructures probed by X-ray magnetic circular dichroism (XMCD) in total electron yield mode. XMCD results for a 3/3/3 heterostructure measured at the **a** Mn L-edge and the **b** Cr L-edge at 15 K. Normalized applied magnetic field dependence of the XMCD signal measured at **c** the Mn L-edge and **d** the Cr L-edge for the 3/3/3 sample. **e** Temperature-dependent XMCD results for a 3/6/3 heterostructure at the Mn L-edge. **f** Comparison of the magnitude of temperature-dependent XMCD signal at the Mn and Cr L-edges in an 0.5 Tesla magnetic field applied in the plane of the sample for a 3/6/3 sample. The Cr data are multiplied by a factor of 5 for clarity

SQUID measurements in Fig. 2b indicative of a coupling of the magnetic moments within the LSMO and LSCO layers.

Role of structural coupling at the LSMO/LSCO interface

To determine the contribution of the atomic-scale structure to the enhanced magnetization, synchrotron surface diffraction experiments were performed at the 33ID beamline at the Advanced Photon Source to image the atomic-scale structures of the interface-engineered heterostructures. Crystal truncation rods (CTRs) and superstructure rods were measured to determine the atomic-scale structures and octahedral rotations profiles. The crystalline quality of the 3/N/3 heterostructures is confirmed by the observance of clear Laue oscillations along the off-specular CTRs (Figure S3 in the Supplementary Materials). The CTRs were converted to real-space 3D electron density maps using the coherent Bragg rod analysis (COBRA)²⁰ phase-retrieval technique from, which the layer-resolved atomic positions were extracted and refined using the GenX X-ray fitting algorithm.²⁵ From this analysis, the atomic positions were determined with sub-picometer resolution. The rotation of the oxygen octahedra in the LSMO and LSCO layers leads to a doubling of the perovskite unit cell and half-order rods in reciprocal space. The amplitude of the octahedral rotations are determined from fits to the integer-order crystal truncation rods and the half-order rods measured (Figure S4 of the Supplementary Materials) for the samples.

The converged structure for the 3/3/3 sample is shown in Fig. 4a. Out-of-phase ($a^-a^-c^-$ in the Glazer notation)²⁶ octahedral rotations are observed along the three crystallographic directions for the LSMO and LSCO layers. The in-plane B-O-B ($B = \text{Ti, Cr, Mn}$) bond angles for each layer is shown in Fig. 4b. The bond-angle decreases from 180° in the bulk STO layers to $\sim 162^\circ$ in the LSCO layers adjacent to the STO substrate. Within the LSMO layers, the average Mn-O-Mn bond angle is 166° in agreement with bulk

LSMO. The reduced bond angles in the surface LSCO layers are attributed to a surface relaxation discussed below.

In addition to the octahedral rotations, cation-anion displacements are observed within the BO_2 planes. The layer-resolved displacements, Δ , for the 3/3/3 sample are shown in Fig. 4c. Negative values of Δ indicate oxygen displacements toward the STO substrate relative to the cations z positions. For bulk LSCO and LSMO, $\Delta = 0$. However, Δ increases to an amplitude of 0.15 \AA at top LSCO surface, whereas the displacements in the LSMO layers are found to be suppressed.

To confirm that the suppressed distortions in the LSMO layers encapsulated with LSCO are related to the absence of polar discontinuities at the LSMO interfaces, we compare the layer-resolved lattice cation-anion displacements along the growth direction for a 4 uc LSMO film and a 3/4/3 heterostructure grown on (001) oriented SrTiO_3 are shown in Fig. 5a and Fig. 5b, respectively. The measured crystal truncation rods and half-order Bragg peaks for the 3/4/3 sample are shown in Figure S5 and S6 respectively, of the Supplementary Materials. At the surface of the 4 uc LSMO film and the LSCO cap layer of the 3/4/3 sample, the O anions are displaced toward the substrate relative to the cations. The ionic rumpling decays 3 uc below the film surface in agreement with previous results for a 10 uc LSMO film¹⁴ and uncapped LaNiO_3 films.²⁰ Although polar distortions are observed in the 4 uc LSMO film, the distortions are suppressed in the encapsulated LSMO layers in the 3/3/3 and 3/4/3 samples.

The ionic displacements at the uncapped LSMO film surface are related to a surface electric field which arises owing to the polar MnO_2 -terminated surface with a net $-0.7e$ charge. The decay length for the surface distortions are found to be on the order of 3 uc ($\sim 12 \text{ \AA}$), which is consistent with the enhanced screening length observed for the rare-earth nickelates²⁰ and theoretical predictions for the manganites.^{15,16} For the uncapped LSMO film, the surface ionic rumpling leads to an elongation in the Mn-O bond-length, which is correlated with reduced double-exchange interactions and a suppression of ferromagnetic ordering in the uncapped LSMO film.^{14,16,27}

On the other hand, the polar distortions are suppressed in the LSMO layers encapsulated with LSCO spacers, leading to ferromagnetism in the LSCO/LSMO heterostructures. The measured layer-resolved polar displacements for the 3/4/3 heterostructure shown in Fig. 5b show that the polar distortions are confined to the top LSCO layer. The absence of polar distortions at the LSCO/STO substrate interface may be related to a reduction in the interface polar discontinuity driven by chemical intermixing observed in Fig. 1e. Although the surface distortions may arise due to incomplete surface layers and atomic vacancies, the direction of the distortions point to the surface field as a significant driver for the observed distortions.^{14,20,28}

The structural measurements and XMCD results confirm that the insertion of LSCO spacer layers leads to bulk-like Mn-O bonding and stoichiometric LSMO layers, which are correlated with the stabilization of ferromagnetization in the encapsulated LSMO layers. The elimination of magnetic dead layers in the LSCO/LSMO/LSMO heterostructures is in contrast to the analogous nominally valence-matched $\text{La}_{0.6}\text{Sr}_{0.4}\text{FeO}_3$ (LSFO)/ $\text{La}_{0.6}\text{Sr}_{0.4}\text{MnO}_3$ interface where dead layers still exist.²⁹ At the LSFO/LSMO interface, an inherent charge transfer between Fe and Mn occurs, which hole dopes the LSMO layers leading to AF interfacial LSMO layers.²⁹ This transfer, is reduced at the LSCO/LSMO interface, as evidenced by the ferromagnetic ground state of the 3/N/3 heterostructures.

The magnetization measured by SQUID normalized to the LSMO thickness in Fig. 2a and the transition temperature of the 3/N/3 heterostructures are significantly less than the bulk values of $3.7 \mu_B/\text{Mn}$ and 370 K , respectively. A reduced net SQUID magnetic moment is expected owing to the net negative contribution of the magnetic moments in the LSCO layers measured by XMCD in

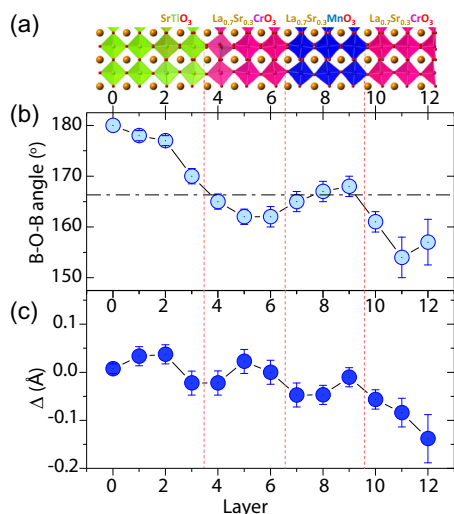


Fig. 4 Atomic-scale structure of a LSCO (3)/LSMO (3)/LSCO (3) heterostructure. **a** Layer-resolved oxygen octahedral rotations of a 3/3/3 heterostructure on SrTiO_3 determined from fits to crystal truncation rods and half-order superstructure rods. **b** Layer-resolved in-plane B-O-B ($B = \text{Ti, Cr, Mn}$) layers 0–3, Cr layers 4–6, Mn layers 7–9, Cr layers 10–12. The dashed line indicates the bulk Mn-O-Mn bond angle for LSMO. **c** Layer-resolved B-O displacements, Δ , along the growth direction for the 3/3/3 heterostructure. Δ represents the displacements in Angstroms, of the oxygen ions relative to the cation (Ti, Mn, Cr) z positions in each layer. Positive Δ are toward the film surface. The error bars are determined from the standard deviation of the atomic positions determined from the fits to the crystal truncation rods

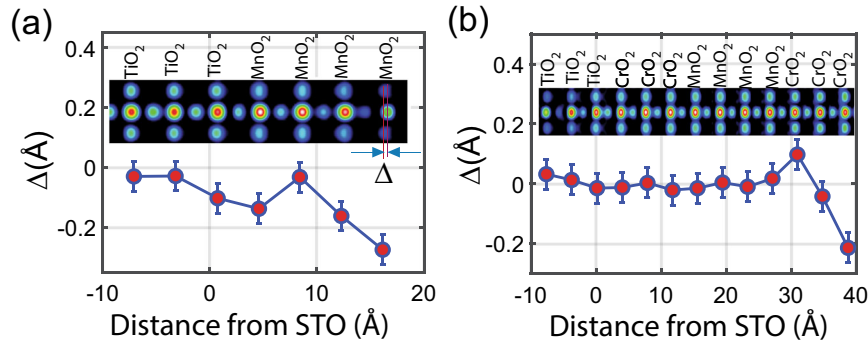


Fig. 5 Layer-resolved polar distortions for LSMO films and LSCO (3)/LSMO (4)/LSCO (3) heterostructures determined from synchrotron X-ray diffraction crystal truncation rod measurements. Layer-resolved ionic displacements for **a** a four-unit cell $\text{La}_{0.7}\text{Sr}_{0.3}\text{MnO}_3$ film and **b** a 3/4/3 sample obtained from synchrotron X-ray crystal truncation rod measurements. The insets show a cut through the measured electron density profiles showing the BO_2 planes and the apical O ions. Δ represents the displacements in Angstroms, of the oxygen ions relative to the cation (Ti,Mn,Cr) z positions. Positive Δ are toward the film surface. The error bars are determined from the standard deviation of the atomic positions determined from Gaussian fits to the electron density maps in the figure insets

addition to the effects of reduced dimensionality of the LSMO layers³⁰ and the effect of epitaxial strain.³¹

Determination of Mn and Cr moments in [LSCO/LSMO] superlattices

For the trilayer samples, the Ti-Cr intermixing at the STO/LSCO interface and the surface distortions observed in the surface LSCO layers are expected to affect the contribution of the LSCO layers to the total magnetization. Hence, to determine the layer-averaged magnetic moments of the LSMO and the LSCO layers, [LSCO (2)/LSMO (N)] superlattice samples were grown by molecular beam epitaxy on (001)-oriented STO substrates where the contributions of the interfacial and surface LSCO layers to the total magnetization is minimized. Representative STEM-EDS analysis of the [2/3] $\times 8$ sample is shown in Fig. 6(a) indicating a well-ordered structure with Cr-Mn intermixing on the order of a unit cell. Crystal truncation rod measurements along the specular and non-specular rods indicate coherently strained epilayers (Figure S7 of Supplementary Materials).

The magnetization for the [LSCO (2)/LSMO (N)] superlattices measured by SQUID normalized to the LSMO thickness are shown as a function of applied magnetic field at 10 K in Fig. 6b and temperature in Fig. 6c. The total SQUID magnetization per Mn, m^* , decreases with the Mn thickness. By assuming that the total SQUID magnetization is a sum of the moments in the LSMO and LSCO sublattices,

$$m^* = m^{\text{Cr}} \left(\frac{M(\text{LSCO})}{N(\text{LSMO})} \right) + m^{\text{Mn}} \quad (1)$$

where m^{Cr} is the average moment per interfacial Cr ion in LSCO, m^{Mn} is the average moment per Mn ion in LSMO, and $M(\text{LSCO})$ and $N(\text{LSMO})$ are the number of LSCO and LSMO layers, respectively. From the linear fit to the measured m^* as a function of $\frac{M(\text{LSCO})}{N(\text{LSMO})}$ shown in Fig. 6d for $M = 2$ and $N \leq 5$, we determine the vertical intercept, $m^{\text{Mn}} = 3.4 \mu_{\text{B}}/\text{Mn}$, which is close to the bulk value of $3.7 \mu_{\text{B}}/\text{Mn}$ and the slope, $m^{\text{Cr}} = -2.1 \mu_{\text{B}}/\text{Cr}$.

A reduction in m^{Mn} can be expected if confinement and the observed interfacial magnetic interactions lead to AF ordering and/or spin canting within the LSMO layers.^{19,29,32} The model for the LSCO/LSMO heterostructure assumes that m^{Mn} and m^{Cr} are independent of the film thickness for $M \leq 2$ and $N \leq 5$. The linear dependence of m^* on $\frac{M(\text{LSCO})}{N(\text{LSMO})}$ in Fig. 6d is consistent with this assumption. In addition, we find that the Mn XMCD signal for a 3/2/3 and 3/3/3 heterostructure (Figure S2b) are identical, in agreement with the assumption above.

To further validate the model described above, we compare two LSCO/LSMO heterostructures where the ratio of LSMO thickness to the LSCO thickness is 2:1. The magnetization as a function of temperature and magnetic field is measured for [LSCO (1)/LSMO (2)] $\times 10$ and [LSCO (2)/LSMO (4)] $\times 6$ superlattice (see Figure S8). The transition temperatures and total magnetic moments are very close in these two configurations. Considering a moment of $-2.1 \mu_{\text{B}}/\text{Cr}$ and a $3.4 \mu_{\text{B}}/\text{Mn}$ obtained from the linear fit in Fig. 6d gives $m^* = 2.245 \mu_{\text{B}}/\text{Mn}$ for $[1/2] \times 10$ and $m^* = 2.17 \mu_{\text{B}}/\text{Mn}$ for $[2/4] \times 6$ superlattice in agreement with the measured magnetization in Figure S8 of the Supplementary materials.

First principles theory

To understand the magnetic coupling of the LSCO (M)/LSMO (N) heterostructures, we perform DFT calculations using the Perdew–Burke–Ernzerhof exchange-correlation formalism³³ using Quantum Espresso³⁴ and ultrasoft pseudopotentials;³⁵ we estimate the magnetic moment of the various heterostructures by comparing the Lowdin projected magnetic moment for the bulk—for which the total available spin is known—with the moment in the superlattices. (For details on the calculations, the estimation of the magnetic moment, and the calculation's limitations, see the Materials and Method section.)

In order to focus on the interfacial magnetism, we perform calculations for a [2/2] superlattice using a collinear spin model imposing a FM state in LSMO as well as a FM state in LSCO, however with the two materials' spins aligned and anti-aligned. We find that the AF coupled state (i.e., LSMO spins anti-aligned with LSCO) is ~ 50 meV lower in energy compared with the FM-coupled state (i.e., LSMO spins aligned with LSCO), in agreement with the experimentally determined AF coupling between the LSMO and LSCO layers. Next, we provide an estimate for the change in the Mn magnetic moment owing to heterostructuring. In bulk FM LSMO, the spin available per Mn in a formula unit of LSMO is predicted to be $3.7 \mu_{\text{B}}/\text{Mn}$ and for bulk LSCO the Cr available moment is estimated to be $2.7 \mu_{\text{B}}/\text{Cr}$. For the [2/2] fully FM ordered superlattice we estimate a Mn moment of $3.61 \mu_{\text{B}}/\text{Mn}$ and $2.83 \mu_{\text{B}}/\text{Cr}$ in the [2/2] calculation, whereas for the calculation in which the two materials have their spins anti-aligned with each other but FM within the same material, we estimate $3.48 \mu_{\text{B}}/\text{Mn}$ and $-2.81 \mu_{\text{B}}/\text{Cr}$.

The theoretical Cr magnetic moment is overestimated compared with the experiment: this is likely because our calculations are done by treating the spins in the approximation that they are collinear (rather than non-collinear).³⁶ For the experimental results discussed above, it is likely the spins on the Cr atoms suffer from frustration due to a competition between two magnetic interactions. The first coupling is across the interface with the Mn where

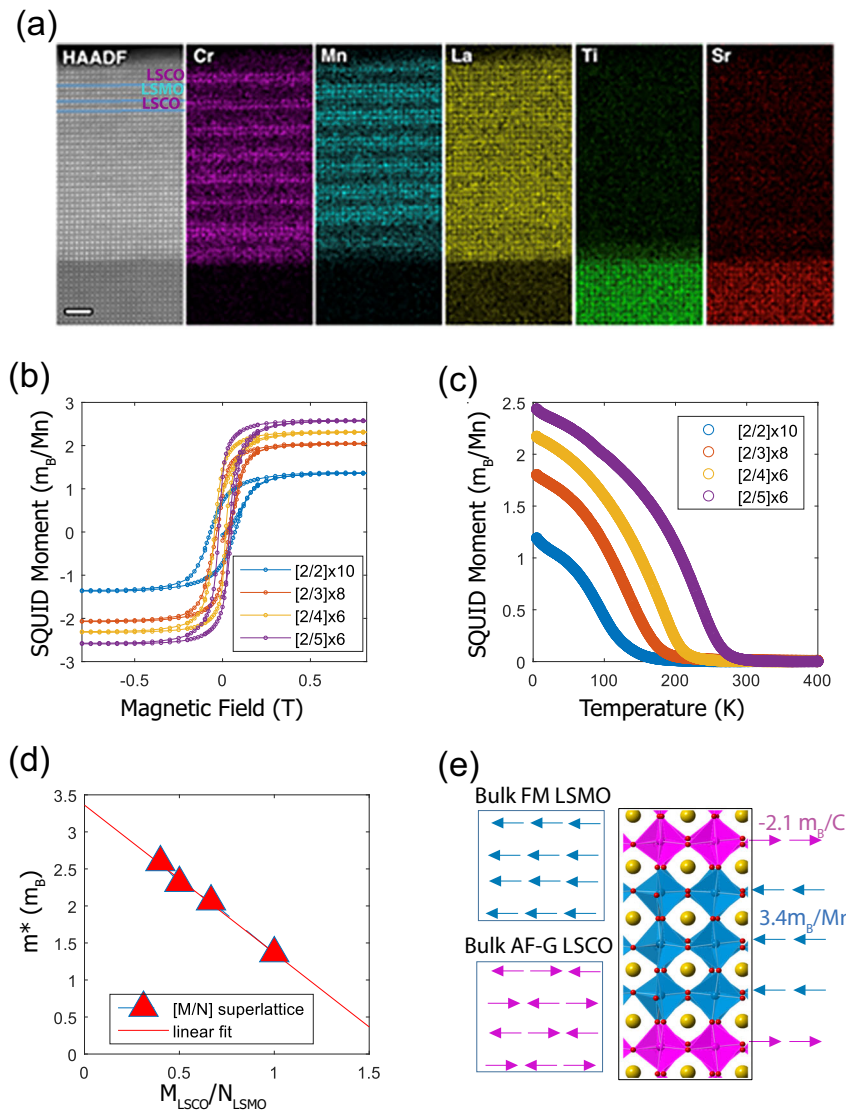


Fig. 6 Magnetic properties of [LSCO (M)/ LSMO (N)] superlattice samples. **a** HAADF-STEM image and EDS map of [2/3]x8 sample. The scale bar represents 2 nm. **b** Field dependence at 10 K of the magnetic moment measured by SQUID normalized to the total LSMO thickness. **c** Temperature dependence of the SQUID magnetization normalized to the total LSMO thickness. **d** SQUID magnetization at 10 K normalized to the total LSMO thickness, m^* , as a function of the ratio of the LSCO and LSMO thickness. The magnetic moment per Mn is determined from the intercept of the linear fit with the vertical axis to be $3.4 \pm 0.1 \mu_B/\text{Mn}$. The magnetic moment per Cr is determined from the slope of the linear fit to be $-2.1 \pm 0.1 \mu_B/\text{Cr}$. **e** Model of the magnetization for bulk LSMO and LSCO and along the growth direction in the LSCO/LSMO heterostructures below the Curie temperature

the interfacial Cr atoms are anti-aligned with the FM Mn atoms at the interface. The second effect is the coupling within LSCO itself which in the bulk is of AFM-G-type.¹⁷

DISCUSSION

Based on the Goodenough–Kanamori rules, a FM superexchange interaction is expected between $\text{Mn}^{3+}(d^4, t_{2g}^3 e_g^1)$ and $\text{Cr}^{3+}(d^3, t_{2g}^3 e_g^0)$ owing to e_g^0 – e_g^1 interactions as has been observed in $\text{LaMn}_x\text{Cr}_{1-x}\text{O}_3$.³⁷ Confinement and the tensile epitaxial strain imposed by the STO substrate will lead to a lifting of the degeneracy of the Mn e_g orbitals where the half-filled $\text{Mn}^{3+} e_g(x^2-y^2)$ point toward the in-plane $\text{Mn}^{4+}(d^3, t_{2g}^3 e_g^0)$ orbitals and the empty $e_g(3z^2-r^2)$ orbitals point out-of-plane towards the LSCO layers. The in-plane Mn^{3+} – Mn^{4+} exchange will be FM, whereas the interfacial superexchange interaction between the empty $\text{Mn}^{4+} e_g(3z^2-r^2)$ orbital and the Cr^{3+} will be AF as experimentally observed. This scenario is consistent with reports on bulk

$\text{La}_{0.7}\text{Ca}_{0.3}\text{Mn}_{1-x}\text{Cr}_x\text{O}_3$ where a significant decrease in the net magnetic moment is observed on increasing the Cr content.³⁸ Competition between these interactions leads to a net AFM coupling between the interfacial LSMO and LSCO layers as evidenced by the XMCD results and exchange bias demonstrated by hysteresis loops.^{39,40} The competing interactions is consistent with a decrease in the Curie temperature as the FM LSMO thickness is reduced.

We note that reduced moments in the thinner LSMO layers may be attributed to charge transfer between the Cr and Mn ions at the LSCO/LSMO interface. To investigate the Cr charge states, we measured the chemical shifts of X-ray absorption near-edge spectra at the Cr K-edge of the [LSCO(2)/LSMO(5)] heterostructure relative to a Cr metal standard (see Figure S9 of the Supplementary Materials). The Cr oxidation state is determined to be $+3.3 \pm 0.1$, which is expected for a stoichiometric $\text{La}_{0.7}\text{Sr}_{0.3}\text{CrO}_3$.⁴¹ However, within the experimental error, it is likely that the transfer of holes from Cr to Mn will lead to a reduction of the Mn

moment and an increase in the Cr^{3+} content at the interface further favoring the AF Mn-Cr exchange. The Cr ELNES (Figure S10) averaged for each layer in the superlattice remains unchanged through the thickness of the film, supporting XAS oxidation state observations.⁴² In addition, we do not observe chemical shifts at the Mn K-edge for the [LSCO (M)/LSMO (N)] superlattices compared with a bulk-like 30 uc LSMO film, which confirms that the growth conditions and heterostructuring do not lead to significant changes in the stoichiometry and charge states of the LSMO layers. This observation is confirmed by the EELS white line ratio for the $[2/3] \times 8$ samples in supplementary Figure S10, which shows little variation in the white line ratio across the film indicating a near constant Mn valence across the film.^{10,42,29}

In conclusion, we have demonstrated the confinement of magnetism in atomically thin LSMO layers by inserting spacer layers, which effectively compensate the interfacial and surface polar discontinuities on (001)-oriented STO substrates. By choosing LaSrCrO_3 as a spacer layer, we also reduce the interfacial oxygen octahedral rotation mismatch¹⁸, leading to bulk-like Mn-O bonding that favors long range ferromagnetic ordering in the LSMO layers. This approach effectively removes structural distortions related to the magnetically dead interfacial layers leading to enhanced ferromagnetism in 2 uc-thick LSMO films encapsulated with LSCO spacers. XMCD measurements indicate AF coupling between the ferromagnetic LSMO films and the interfacial Cr layers, which also contributes to the stabilization of 2D magnetism in the LSMO films. The interfacial AF coupling leads to a magnetic exchange bias as evidenced by SQUID measurements. The ability to engineer the electrostatic and structural boundary conditions at oxide interfaces has important implications for engineering exotic phenomena in two-dimensional oxide systems and the design of nanoscale devices. The observed relation between the interfacial polar distortions on the magnetic properties of the LSMO layers has important implications in the design of multiferroic materials where the electric field effect may be used to modulate the magnetization of the ultrathin oxide layers.

METHODS

Sample preparation

The LSCO layers and the LSMO films were grown at 800°C in 3×10^{-6} Torr atomic oxygen from an oxygen plasma source on TiO_2 -terminated SrTiO_3 (Crystec) substrates by molecular beam epitaxy. The films were grown by co-deposition from effusion cells at a growth rate of ~ 1 unit cell per minute. After growth, the samples were slowly cooled down at $5^\circ\text{C}/\text{min}$ in 5×10^{-6} Torr oxygen in the growth chamber to ensure complete oxidation. The film thickness and surface crystallinity were monitored in situ by reflection high energy electron diffraction (RHEED).

Electron microscopy

Electron microscopy samples were prepared by conventional cross-section mechanical polishing and argon ion milling. Aberration-corrected high-angle annular dark-field-scanning transmission electron microscopy (HAADF-STEM) imaging and energy-dispersive X-ray spectroscopy (EDS) were performed using a FEI Titan G2 60–300 kV operated at 200 kV with a convergence semi-angle of 19.6 mrad . The electron beam was monochromated to achieve 0.4 eV energy resolution and a dispersion of $0.05\text{ eV}/\text{channel}$ was used. Electron energy loss spectroscopy (EELS) was performed to determine the variation of Cr and Mn valence by tracking three spectral features across the LSCO/LSMO heterostructure: the energy loss near-edge fine structure (ELNES), the energy shift of the L-edges, and the L_3/L_2 integrated white line ratio (WLR).^{22,42} EELS data were collected by acquiring 2D spectrum images of the film at a sampling rate of $\sim 1\text{ \AA}/\text{pixel}$.

SQUID magnetization measurements

The magnetic properties of the LSMO thin films and M/N/M heterostructures and [M/N] superlattices were characterized using a Quantum Design SQUID system. The temperature-dependent magnetization curves were measured on warming in an applied in-plane field of 1 KOe .

Synchrotron diffraction measurements

Synchrotron surface diffraction experiments were performed at the 33ID beamline at the Advanced Photon Source to image the atomic-scale structures of the interface-engineered heterostructures using an incident X-ray energy of 15.5 KeV . The samples were mounted in a Be-dome chamber and pumped down to $< 10^{-4}$ Torr. Crystal truncation rods (CTRs) and superstructure rods were measured on each sample and analyzed using the coherent Bragg rod analysis (COBRA) phase-retrieval technique. The atomic positions and occupations obtained from the COBRA-determined electron density maps were refined using the GenX genetic fitting algorithm. For each fitting parameter used in the structural refinement (atomic position, occupation, Debye Waller factor), the error bars were obtained by determining the change in the converged value which leads to a 5% increase in the optimal crystallographic R1 factor.

Soft X-ray XAS and XMCD measurements

Soft XMCD measurements at the Mn and Cr $\text{L}_{2,3}$ absorption edges at were performed at the 4.0.2 beamline at the Advanced Light Source using total electron yield. A magnetic field of 0.5 Tesla was applied parallel to the sample surface.

Density functional theory methodology

The DFT calculations have been performed using the Quantum Espresso code³⁴ using the PBE exchange-correlation functional³³ and ultrasoft pseudopotentials³⁵ using a k-mesh of $7 \times 7 \times 5$ for the bulk 20 atom unit cell and $7 \times 7 \times 3$ for the 40 atom superlattices. For a $c(2 \times 2) \times 2$ 20 atom unit cell for LSMO we obtain an in-plane lattice constant of 3.90 \AA and simulate the strain to the STO lattice constant by imposing an in-plane lattice constant of 3.905 \AA on the superlattices.

For bulk LSMO, we correctly obtain a ferromagnetic ground state. However, for the LSCO we obtain AFM-C instead of AFM-G as the ground state. For a 20-atom unit cell, we find that the AFM-G state is 24 meV higher than AFM-C; whereas the AFM-A state is 86 meV and FM state is 213 meV higher than AFM-C. It is likely that the issues in LSCO calculations are owing to the fact that we are using a collinear spin calculation, as applying a U did not stabilize the AFM-G ground state and previous studies have used a non-collinear spin calculation to correctly predict the AFM-G ground state. Finally, we need a correct way to estimate the local magnetic moment of the atoms, as we notice that in bulk STO-strained LSMO, the magnetic moment calculated on the Mn site using Lowdin orbital projections is $3.35\text{ }\mu_B/\text{Mn}$, a lower number than the experimentally expected one, and lower than what would obtain by dividing the total magnetization of the unit cell by the number of Mn sites, a number, which is exactly $3.7\text{ }\mu_B/\text{Mn}$. This is the owing to the fact that the Lowdin d orbitals of Mn are not sufficient to obtain a complete representation of the valence bands of LSMO and the resulting magnetic moment. We also find that a five-atom formula unit of LSCO has $2.7\text{ }\mu_B/\text{Cr}$ in a FM calculation, with the projected moment on the Cr atoms of $2.43\text{ }\mu_B/\text{Cr}$.

To estimate the magnetic moment of the LSMO and LSCO in the [LSCO (2)/LSMO(2)] heterostructure, we consider the projected magnetic moment onto the d-shells. In the FM-coupled [LSCO(2)/LSMO(2)] heterostructure the projected moment of the Mn atom is $3.25\text{ }\mu_B/\text{Mn}$ and that of the Cr is $2.55\text{ }\mu_B/\text{Cr}$, a small reduction in the magnetic moment of the Mn and a small increase in that of the Cr compared with the FM bulk calculations for the two materials. Assuming the change in magnetic moment obtained using Lowdin projectors is directly proportional to the change per unit cell, we estimate the moments per five atom cell to be $3.59\text{ }\mu_B/\text{Mn}$ and $2.83\text{ }\mu_B/\text{Cr}$. Using this prediction, the prediction for the total magnetization for the heterostructure is $25.68\text{ }\mu_B$, which compares well with the computed total magnetization of $25.60\text{ }\mu_B$. Similarly, for the AFM computed structure, we obtain a projected moment of $3.16\text{ }\mu_B/\text{Mn}$ and $2.53\text{ }\mu_B/\text{Cr}$, which would translate into a moment of $3.49\text{ }\mu_B/\text{Mn}$ —similar to the experiment, and $2.81\text{ }\mu_B/\text{Cr}$, higher than measured in the experiment. The error here is larger than in previous calculations: the total moment per calculation is $2.72\text{ }\mu_B/\text{cell}$, whereas the calculated total moment is $3.11\text{ }\mu_B/\text{cell}$, with an estimated error of $0.05\text{ }\mu_B/\text{formula unit}$ in the estimation.

DATA AVAILABILITY

The data used in the study are available in the manuscript and supplementary data. Raw data files related to this manuscript may be requested from the corresponding author

ACKNOWLEDGEMENTS

D.P.K. and S.K. acknowledge financial support by the US National Science Foundation under Grant No. NSF DMR-1751455. A.N.P. and J.M.L. acknowledge support from the National Science Foundation under Grant No. DMR-1350273. This research used resources of the Advanced Light Source, which is a DOE Office of Science User Facility under contract no. DE-AC02-05CH11231. Use of the Advanced Photon Source was supported by the US Department of Energy, Office of Science, Office of Basic Energy Sciences, under Contract No. DE-AC02-06CH11357. The Flatiron Institute is a division of the Simons Foundation. This work was performed in part at the Analytical Instrumentation Facility (AIF) at North Carolina State University, which is supported by the State of North Carolina and the National Science Foundation (award number ECCS-1542015). The AIF is a member of the North Carolina Research Triangle Nanotechnology Network (RTNN), a site in the National Nanotechnology Coordinated Infrastructure (NNCI). A.B.G. acknowledges discussions with A.J. Millis and A. Georges and support from the Flatiron Institute's Scientific Computing Core.

AUTHOR CONTRIBUTIONS

D.P.K. conceived and supervised the project. D.P.K. and S.K. performed the synchrotron diffraction measurements and analyzed the data and drafted the manuscript. S.K. fabricated the samples and performed the magnetization measurements. A.B.G. performed the theoretical calculations. E.A. and D.P.K. performed the synchrotron spectroscopy measurements and analyzed the data. A.N.P. and J.M.L. performed the electron microscopy measurements.

ADDITIONAL INFORMATION

Supplementary Information accompanies the paper on the *npj Quantum Materials* website (<https://doi.org/10.1038/s41535-019-0164-1>).

Competing interests: The authors declare no competing interests.

Publisher's note: Springer Nature remains neutral with regard to jurisdictional claims in published maps and institutional affiliations.

REFERENCES

- Hwang, H. Y. et al. Emergent phenomena at oxide interfaces. *Nat. Mater.* **11**, 103–113 (2012).
- Reiner, J. W., Walker, F. J. & Ahn, C. H. Atomically engineered oxide interfaces. *Science* **323**, 1018–1019 (2009).
- Sun, J. Z., Abraham, D. W., Rao, R. A. & Eom, C. B. Thickness-dependent magnetotransport in ultrathin manganite films. *Appl. Phys. Lett.* **74**, 3017–3019 (1999).
- King, P. D. C. et al. Atomic-scale control of competing electronic phases in ultrathin LaNiO_3 . *Nat. Nanotechnol.* **9**, 443–447 (2014).
- Scherwitzl, R. et al. Metal-insulator transition in ultrathin LaNiO_3 films. *Phys. Rev. Lett.* **106**, 246403 (2011).
- Vaz, C. A. F., Walker, F. J., Ahn, C. H. & Ismail-Beigi, S. Intrinsic interfacial phenomena in manganite heterostructures. *J. Phys. Condens. Matter* **27**, 123001 (2015).
- Yamada, Y. et al. Polaron ordering in low-doping $\text{La}_{1-x}\text{Sr}_x\text{MnO}_3$. *Phys. Rev. Lett.* **77**, 904 (1996).
- Hwang, H., Palstra, T., Cheong, S.-W. & Batlogg, B. Pressure effects on the magnetoresistance in doped manganite perovskites. *Phys. Rev. B* **52**, 15046 (1995).
- Chen, H. & Ismail-Beigi, S. Ferroelectric control of magnetization in $\text{La}_{1-x}\text{Sr}_x\text{MnO}_3$ manganites: a first-principles study. *Phys. Rev. B* **86**, 024433 (2012).
- Hellman, F. et al. Interface-induced phenomena in magnetism. *Rev. Mod. Phys.* **89**, 025006 (2017).
- Huijben, M. et al. Critical thickness and orbital ordering in ultrathin $\text{La}_{0.7}\text{Sr}_{0.3}\text{MnO}_3$ films. *Phys. Rev. B* **78**, 094413 (2008).
- Boschker, H. et al. Preventing the reconstruction of the polar discontinuity at oxide heterointerfaces. *Adv. Funct. Mater.* **22**, 2235–2240 (2012).
- Kourkoutsis, L. F., Song, J. H., Hwang, H. Y. & Muller, D. A. Microscopic origins for stabilizing room-temperature ferromagnetism in ultrathin manganite layers. *Proc. Natl Acad. Sci. USA* **107**, 11682–11685 (2010).
- Koohfar, S. et al. Structural distortions at polar manganite interfaces. *Phys. Rev. B* **96**, 024108 (2017).
- Burton, J. & Tsymbal, E. Evolution of the band alignment at polar oxide interfaces. *Phys. Rev. B* **82**, 161407 (2010).
- Pruneda, J. et al. Ferrodistortive instability at the (001) surface of half-metallic manganites. *Phys. Rev. Lett.* **99**, 226101 (2007).
- Tezuka, K. et al. Magnetic and neutron diffraction study on perovskites $\text{La}_{1-x}\text{Sr}_x\text{CrO}_3$. *J. Solid State Chem.* **141**, 404–410 (1998).
- Liao, Z. et al. Thickness dependent properties in oxide heterostructures driven by structurally induced metal–Oxygen hybridization variations. *Adv. Funct. Mater.* **27**, 1606717 (2017).
- Moon, E. et al. Structural “ δ doping” to control local magnetization in isovalent oxide heterostructures. *Phys. Rev. Lett.* **119**, 197204 (2017).
- Kumah, D. P. et al. Tuning the structure of nickelates to achieve two-dimensional electron conduction. *Adv. Mater.* **26**, 1935–1940 (2014).
- Zhang, K. et al. Hole-induced insulator-to-metal transition in $\text{La}_{1-x}\text{Sr}_x\text{CrO}_3$ epitaxial films. *Phys. Rev. B* **91**, 155129 (2015).
- Tan, H., Verbeeck, J., Abakumov, A. & Van Tendeloo, G. Oxidation state and chemical shift investigation in transition metal oxides by EELS. *Ultramicroscopy* **116**, 24–33 (2012).
- Gibert, M., Zubko, P., Scherwitzl, R., Íñiguez, J. & Triscone, J.-M. Exchange bias in LaNiO_3 – LaMnO_3 superlattices. *Nat. Mater.* **11**, 195–198 (2012).
- Ding, J. et al. Interfacial spin glass state and exchange bias in manganite bilayers with competing magnetic orders. *Phys. Rev. B* **87**, 054428 (2013).
- Björck, M. & Andersson, G. GenX: an extensible X-ray reflectivity refinement program utilizing differential evolution. *J. Appl. Cryst.* **40**, 1174–1178 (2007).
- Glazer, A. The classification of tilted octahedra in perovskites. *Acta Crystallogr. B* **28**, 3384–3392 (1972).
- Millis, A. Lattice effects in magnetoresistive manganese perovskites. *Nature* **392**, 147–150 (1998).
- Ruf, J., King, P., Nascimento, V., Schlom, D. & Shen, K. Surface atomic structure of epitaxial LaNiO_3 thin films studied by in situ LEED-I (V). *Phys. Rev. B* **95**, 115418 (2017).
- Kumigashira, H. et al. Inherent charge transfer layer formation at $\text{La}_{0.6}\text{Sr}_{0.4}\text{FeO}_3/\text{La}_{0.6}\text{Sr}_{0.4}\text{MnO}_3$ heterointerface. *Appl. Phys. Lett.* **84**, 5353–5355 (2004).
- Dürr, W. et al. Magnetic phase transition in two-dimensional ultrathin Fe films on Au (100). *Phys. Rev. Lett.* **62**, 206–209 (1989).
- Pesquera, D. et al. Surface symmetry-breaking and strain effects on orbital occupancy in transition metal perovskite epitaxial films. *Nat. Commun.* **3**, 1189 (2012).
- Izumi, M. et al. Insulator-metal transition induced by interlayer coupling in $\text{La}_{0.6}\text{Sr}_{0.4}\text{MnO}_3/\text{SrTiO}_3$ superlattices. *Phys. Rev. B* **64**, 064429 (2001).
- Perdew, J. P., Burke, K. & Ernzerhof, M. Generalized gradient approximation made simple. *Phys. Rev. Lett.* **77**, 3865–3868 (1996).
- Giannozzi, P. et al. QUANTUM ESPRESSO: a modular and open-source software project for quantum simulations of materials. *J. Phys.: Condens. Matter* **21**, 395502 (2009).
- Vanderbilt, D. Soft self-consistent pseudopotentials in a generalized eigenvalue formalism. *Phys. Rev. B* **41**, 7892–7895 (1990).
- Solov'ev, I., Hamada, N. & Terakura, K. Crucial role of the lattice distortion in the magnetism of LaMnO_3 . *Phys. Rev. Lett.* **76**, 4825–4828 (1996).
- Zhou, J.-S. et al. Intrinsic structural distortion and superexchange interaction in the orthorhombic rare-earth perovskites RCrO_3 . *Phys. Rev. B* **81**, 214115 (2010).
- Cabeza, O. et al. Magnetization and resistivity in chromium doped manganites. *J. Phys. Condens. Matter* **11**, 2569 (1999).
- Kanamori, J. Superexchange interaction and symmetry properties of electron orbitals. *J. Phys. Chem. Solids* **10**, 87–98 (1959).
- Studer, F., Toulemonde, O., Goedkoop, J., Barnabe, A. & Raveau, B. Magnetic moments in (Cr and Ni) doped CMR manganites as seen by soft X-ray magnetic circular dichroism. *Jpn. J. Appl. Phys.* **38**, 377 (1999).
- Arcon, I., Mirtic, B. & Kodre, A. Determination of valence states of chromium in calcium chromates by using X-ray absorption near-edge structure (XANES) spectroscopy. *J. Am. Ceram. Soc.* **81**, 222–224 (1998).
- Daulton, T. L. & Little, B. J. Determination of chromium valence over the range Cr (0)–Cr (VI) by electron energy loss spectroscopy. *Ultramicroscopy* **106**, 561–573 (2006).



Open Access This article is licensed under a Creative Commons Attribution 4.0 International License, which permits use, sharing, adaptation, distribution and reproduction in any medium or format, as long as you give appropriate credit to the original author(s) and the source, provide a link to the Creative Commons license, and indicate if changes were made. The images or other third party material in this article are included in the article's Creative Commons license, unless indicated otherwise in a credit line to the material. If material is not included in the article's Creative Commons license and your intended use is not permitted by statutory regulation or exceeds the permitted use, you will need to obtain permission directly from the copyright holder. To view a copy of this license, visit <http://creativecommons.org/licenses/by/4.0/>.

© The Author(s) 2019